Underthrusting linked to closure of the Rocas Verdes Basin: insights from Turonian/Coniacian satellite plutons, Isla Capitán Aracena, southern Patagonia, Chile

Gianfranco Gregorina[1], Fernanda Torres-Mancinelli[2], *Mauricio Calderón[3], Cristóbal Ramírez de Arellano[1], C. Mark Fanning[4], Thomas Theye[5], Joachim Opitz[5], Diego Rojo[6], Gonzalo Galaz[7]

[1]Escuela de Ciencias de la Tierra, Universidad Andres Bello, Av. República 220, Santiago, Chile

[2]Department of Tectonics and Resources, Institute of Geoscience, Ruhr-Universität Bochum, Universitätsstr. 150, 44801 Bochum, Germany

[3]Carrera de Geología, Facultad de Ingeniería, Universidad del Desarrollo, Av. Plaza 680, Las Condes, Chile

[4]Research School of Earth Sciences, The Australian National University, Canberra, ACT 2601, Australia

[5]Institut für Anorganische Chemie, Universität Stuttgart, Pfaffenwaldring 55, Stuttgart D-70569, Germany

[6]Instituto de Estudios Andinos IDEAN (Universidad de Buenos Aires - CONICET), Buenos Aires, Argentina

[7]Departamento de Geología, Universidad de Atacama, Av. Copayapu 485, Copiapó, Chile

**Corresponding author.*

g.gregorina96@gmail.com (G. Gregorina), mfernanda.torres.g@gmail.com (F. Torres), mccaldera@gmail.com (M. Calderón), cristobal.ramirez@unab.cl (C. Ramírez de Arellano), cmarkfanning@gmail.com (C.M. Fanning), thomas.theye@imi.uni-stuttgart.de (T. Theye), joachim.opitz@imi.uni-stuttgart.de (J. Opitz), d.rojomartel@gmail.com (D. Rojo), gonzalo.galaz@uda.cl (G. Galaz).

Abstract

The Petite and Mercurio satellite plutons of the Patagonian Batholith intrude folded marine sedimentary successions and ophiolitic sequences within the Magallanes fold-and-thrust belt on Isla Capitán Aracena (~54° S), south of the Cenozoic transcurrent Magallanes-Fagnano Fault System. Their petrogenesis and tectonic significance were investigated through an integrated approach combining field observations, U-Pb zircon geochronology, whole-rock geochemistry, mineral chemistry and thermobarometry. Zircons from three samples of hornblende-bearing diorite and quartz diorite yielded Turonian/Coniacian crystallisation ages (90±1 Ma). They display calc-alkaline, metaluminous compositions, enrichment in Light Rare Earth Elements, and negative Nb-Ta-Ti anomalies, consistent with subduction-modified mantle sources in continental magmatic arcs. The compositions of amphibole, classified as magnesio-hornblende and tschermakitic hornblende, record crystallisation temperatures of ~800–850 °C and pressures of ~3-3.5 kbar (~10 km depth) in moderately oxidizing, hydrous magmas. Collectively, these data suggest that the Petite pluton was derived from water-saturated basaltic-andesite magmas whose compositions evolved through clinopyroxene and plagioclase fractionation, promoting physicochemical conditions conducive to late co-crystallisation of labradorite-andesine plagioclase and hornblende with pronounced Eu and Sr negative anomalies. The new data indicate that the oceanic remnants of the Rocas Verdes back-arc marginal basin were already buried at depths of approximately 10 km by ca. 90 Ma within a fold-and-thrust system developed during the underthrusting of continental crust.

Keywords: Fuegian Batholith, Rocas Verdes Basin, U-Pb zircon dating, amphibole chemistry, Late Cretaceous magmatism.

Enterramiento tectónico asociado al cierre de la Cuenca Rocas Verdes: aportes a partir de plutones satélite del Turoniano/Coniaciano, Isla Capitán Aracena, Patagonia austral, Chile

Resumen

Los plutones satélites Petite y Mercurio del Batolito Patagónico intruyen sucesiones sedimentarias marinas plegadas y secuencias ofiolíticas en la Isla Capitán Aracena (~54° S), en el dominio occidental de la faja plegada y corrida de Magallanes, al sur del sistema de falla transcurrente Magallanes-Fagnano. Su petrogénesis y significado tectónico fueron investigados mediante la combinación de observaciones de campo, geocronología U-Pb en circones, geoquímica de roca total, química mineral y termobarometría. Los circones de tres muestras entregaron edades de cristalización turonianas/coniacianas (90±1 Ma), y las rocas corresponden predominantemente a dioritas y cuarzodioritas de hornblenda. Presentan afinidad calcoalcalina, carácter metaluminoso, enriquecimiento en tierras raras livianas y anomalías negativas de Nb-Ta-Ti, consistentes con fuentes mantélicas modificadas por subducción en arcos magmáticos continentales. La composición de cristales de anfíbola, clasificada como magnesio-hornblenda y hornblenda tschermakítica, registra temperaturas de cristalización de ~800–850 °C y presiones de ~3–3,5 kbar (~10 km de profundidad) a partir de magmas hidratados y moderadamente oxidantes. En conjunto, estos datos sugieren que el plutón Petite derivó de magmas andesítico-basálticos saturados en agua, cuya composición evolucionó mediante fraccionamiento de clinopiroxeno y plagioclasa, promoviendo condiciones fisicoquímicas favorables para la co-cristalización de plagioclasa de tipo labradorita-andesina y hornblenda con anomalías negativas de Eu y Sr. Los nuevos datos indican que los remanentes oceánicos de la cuenca marginal Rocas Verdes ya se encontraban enterrados a profundidades de aproximadamente 10 km a los ca. 90 Ma, dentro de un sistema de pliegues y cabalgamientos desarrollado durante la subducción de corteza continental.

Palabras clave: Batolito Fueguino, Cuenca Rocas Verdes, dataciones U-Pb en circón, química de anfíbol, magmatismo Cretácico tardío.

1. Introduction

The Patagonian and Fuegian Andes are the southernmost segments of the Andean Cordillera, preserving a complex record of Mesozoic to Cenozoic magmatism and deformation associated with the opening and subsequent inversion of the Rocas Verdes Basin and the rise of the southern Andes (Dalziel, 1981; Pankhurst *et al.,* 2000; Stern and de Wit, 2003; Hervé *et al.,* 2007a; Calderón *et al.,* 2013). These magmatic belts consist of a series of diachronous batholiths and back-arc ophiolitic complexes that developed in response to evolving subduction dynamics along the southwestern margin of Gondwana (Fig. 1).

The Rocas Verdes Basin represents a key Mesozoic back-arc extensional system developed along the southern Gondwana margin (Dalziel *et al.,* 1974; Stern and de Wit, 2003; Calderón *et al.,* 2007). Its closure was linked to the opening of the Atlantic Ocean and global changes in tectonic plate configurations, involving Late Cretaceous tectonic emplacement of ophiolitic complexes and intrusion of satellite plutons to the east and north of the main axis of the Patagonian Batholith (Dalziel, 1981; Hervé *et al.,* 2007a; Klepeis *et al.,* 2010; Calderón *et al.,* 2012). The Mesozoic-Cenozoic Patagonian Batholith (Fig. 1), which extends from 40° to 56° S, is among the longest-lived plutonic belts associated with subduction (Hervé *et al.,* 2007a), recording the protracted magmatic evolution of the southern Andean margin.

On Isla Capitán Aracena, map-scale satellite intrusions such as the Petite and Mercurio plutons crosscut the hinterland domain of the Magallanes fold-and-thrust belt, where the Upper Jurassic and Lower Cretaceous Capitán Aracena Ophiolitic Complex are tectonically juxtaposed with marine sedimentary successions of the Yaghan Formation (Fig. 1). The spatial relationship between these plutons and the deformed seafloor remnants of the Rocas Verdes Basin makes them ideal targets to investigate the crustal evolution associated with the tectonic inversion of back-arc marginal basins.

This study investigates the petrogenesis and tectono-magmatic significance of the Petite and Mercurio plutons within the framework of Rocas Verdes Basin inversion, through an integrated approach combining field and petrographic observations, bulk-rock and mineral geochemistry, and geochronology, with a particular focus on amphibole compositional variations. Emphasis is placed on the study of amphibole and plagioclase chemical compositions that can be used as a geothermobarometers and as a proxy for water activity in the melt.

2.Tectono-magmatic setting

The geology of Isla Capitán Aracena was first described by Otzen (1987, unpublished report; compiled in the geological map of Chile by Sernageomin, 2003), who recognized exposures of metasedimentary basement rocks, ophiolitic complexes, and younger intrusive bodies. The protolith of the metasedimentary rocks were turbiditic successions of sandstones and mudstones. U-Pb detrital zircon ages from samples collected on the eastern side of the island (Fig. 1B) indicate a dominant Permian source signature with a more complex sedimentary provenance, involving Neoproterozoic and Mesoproterozoic sources and including a significant component of Grenville-age zircons (Hervé *et al.,* 2010). Overlying this metamorphic basement is the Tobífera Formation, an Upper Jurassic-Lower Cretaceous silicic volcanic succession dominated by subaqueous rhyolitic flows and pyroclastic deposits (Bruhn *et al.,* 1978; Pankhurst *et al.,* 2000). This succession records the onset of crustal extension and back-arc rifting in a supra-subduction setting, which led to the formation of the Rocas Verdes marginal basin (Dalziel *et al.,* 1974; Stern and de Wit, 2003; Calderón *et al.,* 2007).

The oceanic-type crust remnants of the Rocas Verdes Basin, including ophiolitic complexes and related sedimentary successions, are discontinuously exposed from 50° to 55° S (well exposed at Cordillera Sarmiento, Isla Capitán Aracena, and Isla Navarino; Fig. 1A). They include the Sarmiento, Capitán Aracena, and Tortuga ophiolitic complexes (cf. Calderón *et al.,* 2013). The basin was filled by hemipelagic sedimentary rocks of the Upper Jurassic to

Lower Cretaceous Yaghan and Zapata formations (Katz and Watters, 1966; Dott *et al.,* 1977; Allen, 1982; Wilson, 1991; Fildani and Hessler, 2005).

Closure of the Rocas Verdes Basin began during the Aptian-Albian, marking the onset of the Andean orogeny in southern South America (Dalziel, 1981; Hervé *et al.,* 1984; Cunningham, 1993). Progressive tectonic oceanward underthrusting of the back-arc basin floor beneath the island arc continued until the Late Cretaceous, generating an accretionary wedge and fold-and-thrust belt (Hervé *et al.,* 2007b; Klepeis *et al.,* 2010; Fosdick *et al.,* 2011; Calderón *et al.,* 2012; Betka *et al.,* 2015; Torres Carbonell et al 2020; Muller *et al.,* 2021; Gallardo et al., 2022); we refer to this here as the Magallanes fold-and-thrust belt. The transition from extensional to contractional tectonics was accompanied by migration of the arc towards the continent and renewed calc-alkaline magmatism (Hervé *et al.,* 2007a; Torres Garcia *et al.,* 2020; Ramírez de Arellano *et al.,* 2012). Subsequently, Late Cretaceous to Neogene arc magmatism in the Patagonian Batholith accompanied the development of the Magallanes-Austral Basin until the Miocene (Wilson, 1991; Fosdick et al 2011; Gallardo et al., 2022; Stevens Goddard et al., 2023). Since Miocene times, the convergent margin of South America has been affected by the subduction of oceanic ridges and the development of intraplate volcanism associated with asthenospheric windows (D'Orazio *et al.,* 2001; Ramírez de Arellano *et al.,* 2021).

This study focuses on the Petite and Mercurio plutons, located outside the eastern margin of the Patagonian Batholith, which intrude ophiolitic complexes within the internal zone of the Magallanes fold-and-thrust belt. Both record processes of arc magmatism during the tectonic inversion of the Rocas Verdes Basin and onset of Andean orogeny in southern Patagonia.

3. Analytical methods

Twenty-five samples were collected from the Petite and Mercurio plutons and studied through a polarising microscope. Polished thin sections for petrographic and in situ geochemical analysis were prepared by M. Schmelz at Universität Stuttgart.

Zircon grains for U-Pb dating were separated from two samples of the Petite pluton and one of the Mercurio pluton using the standard procedures, including crushing, grinding, Wilfley Table separation, magnetic, and heavy liquid separation, at the commercial laboratory of Juan Vargas, Santiago. Reflected and transmitted light photomicrographs were prepared for all zircon grains, as were cathodoluminescence (CL) Scanning Electron Microscope (SEM) images. These CL images were used to decipher the internal structure of the sectioned grains and to ensure that the ~20μm SHRIMP spot was wholly within a single age component.

The U-Th-Pb analyses were made using a SHRIMP II at the Research School of Earth Sciences at The Australian National University, Canberra, following procedures given in Williams (1998, and references therein). Each analysis consisted of 6 scans through the mass range, with a Temora reference zircon grain analysed for every 3 unknown analyses. The data were reduced using the SQUID Excel Macro of Ludwig (2001). The Pb/U ratios were normalised relative to a value of 0.0668 for the Temora reference zircon, equivalent to an age of 417 Ma (see Black et al., 2003). Uncertainties given for individual analyses (ratios and ages) are at the 1σ level (see data in Table 1). Tera and Wasserburg concordia plots, probability density plots with stacked histograms, and weighted mean age calculations were carried out using ISOPLOT/EX (Ludwig, 2003), the latter reported with 95% confidence limits.

The same three samples were analysed for whole-rock major and trace elements by fusion-ICP-OES (Inductively Coupled Plasma Optical Emission Spectroscopy) and ICP-MS (Inductively Coupled Plasma-Mass Spectrometry) at Actlabs in Vancouver, Canada. All data presented in figures and text were recalculated on a volatile-free basis and are listed in Table 2.

Major element compositions of amphibole, plagioclase, biotite, titanite, K-feldspar, and ilmenite from sample FC1947 (hornblende diorite) were determined at the Institut für Mineralogie und Kristallchemie, Universität Stuttgart, using a Cameca SX100 scanning electron microprobe. Operating conditions were set at 15 kV acceleration voltage and 15 nA beam current for all analyses. Representative electron probe microanalysis (EPMA) data are reported in Table 3.

Trace element compositions of amphibole were determined by laser ablation (LA-ICP-MS) at Institut für Mineralogie und Kristallchemie at the Universität Stuttgart, using an Agilent 7700 ICP-MS coupled to a Teledyne CETAC LSX-213 laser equipment. At 213 nm, the maximum laser energy is 4 mJ (pulse length <5 ns) at a spot diameter of 200 μm. Laser excitation was carried out at 50% energy with a spot diameter of 50 μm and a laser pulse frequency of 10 Hz. The data acquisition was performed using the Agilent MassHunter software (version B.01.01). Each analysis comprised the acquisition of background ion intensities (gas-blank) for roughly 25 s, followed by laser irradiation of the sample spot for roughly 60 s. Background-corrected individual ion intensities were integrated over a selected appropriate interval of the ablation time profile and divided by the integral of the corrected intensity of the selected isotope of the internal reference element. The software used for calibration and data evaluation was developed by J. Opitz (Massonne et al., 2013). DLH7 and DLH8 glasses (P&H Developments Ltd.), as well as NIST SRM 612 and NIST SRM 610 glasses were used as standards. Relative elemental concentrations were calculated from the abundance of the corresponding isotope assuming natural isotope distribution and an individual calibration factor determined under the same experimental conditions. The silicon concentration, as calculated from the ^{29}Si isotope, was used as internal standard and set to the value obtained by EMPA. All LA-ICP-MS data are shown in Table 4.

4. Results

4.1. Field relations and petrography

The Petite and Mercurio plutons intrude the hinterland domain of the Magallanes fold-and-thrust belt, where tectonic slices of ophiolitic complexes and marine sedimentary rocks are juxtaposed (Fig. 1A). The Petite pluton is located north of a reverse fault, here referred to as the Aracena Thrust, whereas the Mercurio pluton lies to the south of this structure (Fig. 1B).

These dioritic to tonalitic bodies are locally deformed satellite plutons outside the main exposure belt of the Patagonian Batholith (Otzen, 1987).

The Petite pluton, exposed at Seno Petite in the northern part of the island (Figs. 1B and 2A), consists of hornblende-bearing diorites and quartz diorites. At outcrop scale it exhibits flow banding characterized by segregated leucocratic layers (Fig. 2B), orientated parallel to the local direction of magmatic flow, probably controlled by tectonic stresses associated with pluton emplacement. The Mercurio pluton, cropping out near Seno Mercurio (Fig. 1B), comprises hornblende-biotite tonalite containing centimetric microdiorite enclaves and late aplitic veins. Two samples from Petite pluton (FC1947 and FC1944) and one sample from the Mercurio pluton (FC1924) were selected for geochronological and geochemical analyses. Samples are briefly described below.

Sample FC1947 (Fig. 2C, D) is a medium- to fine-grained diorite with inequigranular and interlocking textures, locally displaying intrafasciculate, poikilitic, and adcumulate features. The primary mineral assemblage consists of plagioclase (55%), hornblende (30%), biotite (10%), and quartz (5%). Plagioclase is typically unzoned and mostly unaltered, occurring as subhedral tabular crystals with dominant polysynthetic twinning, both in the matrix and as inclusions within hornblende. Hornblende is subhedral, with prismatic to massive habits and greenish to yellowish pleochroism. Biotite is subhedral, while interstitial quartz exhibits undulose extinction. Accessory phases include titanite and zircon. Opaque minerals account for ~5% of the rock. Secondary minerals (~5%) include chlorite, epidote, and actinolite, mainly replacing hornblende and biotite.

Sample FC1944 (Fig. 2E) is a medium- to fine-grained quartz diorite with inequigranular, interlocking, and poikilitic textures showing adcumulate features. The primary mineral assemblage consists of plagioclase (55%), hornblende (25%), biotite (10%), and quartz (10%). Plagioclase occurs as subhedral orientated tabular crystals with dominant polysynthetic and Carlsbad twinning. Hornblende is typically subhedral with a prismatic habit and greenish to yellowish pleochroism. Biotite occurs as anhedral brown flakes, while quartz is anhedral, interstitial, and exhibits undulose extinction. Accessory phases include titanite and zircon. Opaque minerals account for ~5% of the rock. Secondary minerals (~5%) include chlorite, epidote, and actinolite, mainly replacing hornblende and biotite.

Both samples display comparable petrographic features and share a similar distribution of minor and alteration phases. Accessory minerals are represented by titanite and zircon, while opaque phases account for approximately 5% of the rocks. Titanite commonly occurs as inclusions within hornblende or along fractures, whereas fine magnetite-ilmenite intergrowths are typically observed at amphibole-plagioclase interfaces, highlighting consistent late- to post-magmatic processes in both samples.

Sample FC1924 from the Mercurio pluton (Fig. 2F) is a medium- to fine-grained tonalite with inequigranular, interlocking, and locally poikilitic textures. The primary mineral assemblage consists of plagioclase (40%), hornblende (30%), quartz (20%), biotite (5%), and K-feldspar (5%). Plagioclase occurs as subhedral tabular crystals with dominant polysynthetic and subordinate Carlsbad twinning. Hornblende is subhedral to locally euhedral, displaying prismatic habits. Quartz and K-feldspar are mostly anhedral and interstitial, while biotite occurs as subhedral brown flakes. Secondary minerals (~5%) include chlorite, epidote, and actinolite, replacing ferromagnesian phases, whereas feldspars are altered to clay minerals. Opaque minerals account for ~5% of the rock.

4.2. Zircon geochronology

A summary of the new SHRIMP U-Pb zircon age determinations is presented in Table 1. Representative cathodoluminescence (CL) images and Tera-Wasserburg concordia and probability density plots are shown in figure 3.

Hornblende diorite (sample FC1947). The zircons are equant to elongate, lozenge shaped, blocky grains many with pyramidal terminations. Whilst the grains are generally euhedral in shape, the surfaces are often weakly mottled or slightly irregular which is likely the result of a post-primary igneous crystallisation, hydrothermal fluid affecting the grains. The grains are mostly clear under transmitted light but have some inclusions and irregular cavities (see grains 1 and 3 in figure 3A). The grains are around 150-350 μm in length/diameter. The CL images show sector zoning, often from centre to rim. There are some irregularly zoned grains; grain 4 (see figure 3A) has a darker outer area that encloses the lower U central component. Grains 14 and 16 (not shown) appear to have offset, possible inherited central areas enclosed within the dominant sector zoned igneous component.

Seventeen areas were analysed on 16 zircon grains. Th and U contents are generally low to moderate, although somewhat variable: U is mostly between ~70 and ~160 ppm but does range to higher values of ~450 ppm and ~494 ppm in analyses 13.1 and 16.2 respectively (central component to grain 16). The Th/U ratios are in the range ~0.40 to ~0.80, which is consistent with those for normal crustal igneous zircon. The suspected inherited area analysed in grain 16 gives an older $^{206}Pb/^{238}U$ age of ~97 Ma (16.2), apparently recording the presence of earlier zircon crystallisation. Overall, the areas analysed contain small amounts of common Pb and plot above the Tera-Wasserburg concordia curve. The probability density plot of radiogenic $^{206}Pb/^{238}U$ ages (Fig. 3B) shows a dominant simple bell-shaped distribution, with the older area analysed on grain 16 being a clear outlier. The area analysed on grain 4 is also at the older end of that distribution with a $^{206}Pb/^{238}U$ age of ~93.5 Ma. The areas analysed on grains 11 and 12 are slightly younger at ~87 Ma and ~86 Ma respectively; although due to the low U, the analysis of grain 11 is not as well constrained as others. Overall, a weighted mean for the 14 analyses forming the dominant bell-shaped grouping has no excess scatter (MSWD=0.9), giving a $^{206}Pb/^{238}U$ age of 90.0±0.8 Ma. This age constrains the dominant period of igneous zircon crystallisation.

Hornblende quartz diorite (sample FC1944). The zircons are mostly equant to subequant, blocky, euhedral crystals with multifaceted pyramidal outlines. A few grains have irregular inclusions and cavities, and some appear to have been hydrothermally altered with pitted or mottled exterior surfaces. The grains are generally around ~100 to ~300 μm in diameter, but range to at least 350-400 μm in length. The CL images show dominantly sector zoning from centre to rim. In places there is more irregular zoning, mainly associated with the cavities.

Twenty-two grains were analysed. U is low to moderate ranging from ~65 to ~225 ppm with grains 10 and 16 higher at ~330 ppm. Th is consistently lower, between ~25 and 130 ppm, with Th/U ratios in the range ~0.35 to ~0.76. All areas analysed plot close to or within uncertainty of the Tera-Wasserburg concordia. However, they show an asymmetric distribution on a probability density plot of calculated radiogenic $^{206}Pb/^{238}U$ ages, with a tail to the younger age side. Nevertheless, a weighted mean for all 22 analyses has no excess scatter (MSWD=1.1), giving a $^{206}Pb/^{238}U$ age of 89.2±0.6 Ma (i.e., they are all within analytical uncertainty). The areas analysed on grains 9 and 10 (Fig. 3A) are slightly younger and it is possible that these areas have lost a small amount of radiogenic Pb. Both of those spots are close to imperfections in their respective grains. If these two analyses are excluded, the weighted mean $^{206}Pb/^{238}U$ age is 89.6±0.7 Ma (MSWD=0.6). This age is considered the better estimate for the sector zoned igneous zircon crystallisation, albeit within uncertainty of the overall weighted mean calculation.

Hornblende-biotite tonalite (sample FC1924). The zircons are mostly elongate to subequant, euhedral grains, with pyramidal terminations; some with multifaceted terminations. A few irregularly shaped grains are present; for example, grains 2, 17, and others not analysed. A prominent feature of grain 1 is the presence of a ~50–80 μm diameter sulphide inclusion. The grains range to at least 450 μm in length with many around ~200–350 μm. The CL images show predominantly oscillatory zoned interiors, often from centre to rim. In some grains there are homogeneous central areas enclosed within oscillatory zoned outer areas. Grain 16 (Fig. 3A) is anomalous with one end showing simple oscillatory zoning, whilst the other is U rich and has an irregular dark CL response.

Twenty-five areas were analysed on 22 zircon grains. Analysis 16.1 of the dark CL end has anomalously high U at ~1550 ppm. All other areas analysed have moderate U concentrations between ~130 and ~330 ppm, with grain 6 notably lower at ~90 ppm. The Th values are generally low and the Th/U ratios also mostly low between ~0.15 and ~0.50, with the area analysed on grain 2 higher at ~0.74. The 25 areas analysed are mostly dominated by radiogenic Pb and plot close to the Tera-Wasserburg concordia. The homogeneous CL central areas analysed on grains 14, 15, and 16 record similar $^{206}Pb/^{238}U$ ages to the oscillatory zoned outer areas. The probability density plot of radiogenic $^{206}Pb/^{238}U$ ages shows a slightly dispersed bell-shaped distribution, with a slight tail on the younger age side. The analysis of the central area to grain 15 (15.2; Fig. 3A) yields a younger $^{206}Pb/^{238}U$ age of ~86 Ma and the area analysed is considered to have lost some radiogenic Pb. The same is similarly interpreted for the younger analysis of grain 18 at ~86 Ma. A weighted mean for the remaining 23 analyses has no excess scatter (MSWD=0.9). giving a $^{206}Pb/^{238}U$ age of 89.4±0.5 Ma and this constrains the dominant period of igneous zircon crystallisation.

In summary, the three preferred crystallisation age estimates of these samples overlap within analytical error. If they are regarded as registering coeval emplacement within a single magmatic episode, their weighted mean age of 89.6±0.4 Ma can be conservatively reported as 90±1 Ma. This age is indistinguishable from the age of the Turonian-Coniacian boundary at 89.8±0.3 Ma (International Chronostratigraphic Chart v2024/12).

4.3. Bulk-rock major and trace element composition

The hornblende-bearing diorite and quartz diorite from the Petite pluton have low SiO_2 of 48.5 and 54.8 wt%, respectively and moderate Mg# (42–43; calculated as molar Mg/(Mg+Fe)×100). Whereas the hornblende-biotite tonalite from the Mercurio pluton has higher SiO_2 content (63.4 wt%) also with moderate Mg# (52).

The major oxide compositions of the three analysed samples are subalkaline in composition. In the K_2O-SiO_2 diagram (Fig. 4A; Ewart, 1982), the samples plot within the medium-K calc-alkaline field. They also plot within the metaluminous compositional field (Aluminium Saturation Index of 0.78–0.94), consistent with I-type granitoids typically associated with continental arcs settings. For regional comparison, data from Cretaceous plutonic rocks of the South Patagonian Batholith reported by Hervé et al. (2007a), are also plotted in figure 4.

The primitive mantle normalized trace-element diagram (Fig. 4B; Palme and O'Neill, 2014) shows a strong enrichment in large-ion lithophile elements (LILE) such as Ba, Rb, Sr, and K relative to high field strength elements (HFSE) including Nb, Ta, Zr, and Ti. The samples display moderate Ti depletion. Chondrite-normalized rare earth element (REE) patterns (Fig. 4C; Palme and O'Neill, 2014) indicate enrichment in light REE (LREE) relative to heavy REE (HREE), with $(La/Yb)_N$ = 5.9–7.2, comparable to compositions reported for coeval granitoids of the South Patagonian Batholith. The tonalite of the Mercurio pluton exhibits lower total REE contents and a subtle positive Eu anomaly, the Petite pluton samples show slightly higher REE concentrations and negligible negative Eu anomalies.

4.4. Mineral major and trace element composition

Major oxides in minerals from the Petite pluton diorite (sample FC1947), including amphibole, plagioclase, biotite, K-feldspar, titanite, and ilmenite, were analysed (see results in Table 3). Some amphibole grains were selected for in situ analysis of trace element and REE concentrations, which are presented in Table 4. Chemical composition diagrams are shown in figure 5.

Amphibole crystals are characterised by Ca contents in the B site of 1.82–1.93 atoms per formula unit (a.p.f.u.), whereas Na and K in the A site generally range from 0.46 to 0.51 a.p.f.u. Ti contents vary between 0.14 and 0.25 a.p.f.u., with Si ~6.5 and Mg# values between 0.60 and 0.72. According to the classification of Locock (2014; Fig. 5A) these compositions correspond to magnesio-hornblende and tschermakite. Total Al contents (Al_{tot}) range from 1.60 to 1.82 a.p.f.u.

Chondrite-normalised REE patterns in amphibole crystals (Fig. 5B) are nearly flat to slightly convex upward, showing minor LREE enrichment with $(La/Sm)_N$ = 0.78–1.20 and $(Gd/Yb)_N$ = 1.12–1.41, together with a consistent negative Eu anomaly (Eu/Eu* = 0.5–0.8). The chondrite-normalised trace-element compositions (Fig. 5C) show Nb-Ta, Sr, Zr, and Ti negative anomalies.

Plagioclase crystals are predominantly labradorite to andesine ($An_{60–44}$ mol%) and with negligible K_2O contents of 0.05–0.19 wt%. Plagioclase inclusions within the amphibole are labradorite. Biotite is characterized by SiO_2 contents of ~36 wt%, TiO_2 = 3–4 wt%, and Fe#

$(Fe^{2+}/(Fe^{2+}+Mg)) \leq 0.5$. Titanite displays compositional zoning, with Fe-rich rims and Mn-rich cores. Ilmenite is characterised by Mn (0.21 wt%), Ti (0.19 wt%), and Fe (0.51 wt%).

5. Discussion

5.1. Thermobarometry and hygrometry

Amphiboles are stable over a wide range of pressures and temperatures (e.g., Hammarstrom and Zen, 1986; Davidson *et al.,* 2007), making them reliable indicators for the geothermobarometric constraints in subduction-related magmatic systems.

In a first approximation, application of the edenite-richterite thermometer (Holland and Blundy, 1994) yields temperatures between 801 and 863 °C (±40 °C). Consistently, the application of the Putirka (2016) thermometer (developed with experimental data) yields temperatures between 802 and 857 °C (±30 °C). The initial crystallisation temperature of a typical dioritic magma is ~1100 °C but it can extend to 800 °C and slightly lower temperatures in more evolved, hydrous magmas (Pietranik et al., 2009).

The dependence of Al^{VI} in hornblende on pressure is well established (e.g., Hammarstrom and Zen, 1986; Schmidt, 1993, Mutch *et al.,* 2016; Putirka, 2016). Applying the quadratic Al^{VI} pressure relationship proposed by Mutch et al. (2016), the data from hornblende in diorites yield pressures of 3.2–3.4 kbar. The revised Hammarstrom and Zen (1986) calibration of Putirka (2016) produces consistent estimates of 3.1 and 3.4 kbar, reinforcing these pressure constraints, corresponding to hornblende crystallisation at approximately 10 km depth.

The compositional variations in magmatic amphiboles commonly reflect changes in physicochemical parameters such as temperature, pressure, melt water content, and oxygen fugacity (Polzunenkov, 2018). The water content of the silicate melt in thermodynamic equilibrium with amphibole was estimated using the amphibole hygrometer calibration of Ridolfi and Renzulli (2012), indicating a range from 6.0 to 6.5 wt% H_2O. Ridolfi and Renzulli (2012) also developed empirical calibrations relative to the Ni-NiO (NNO) buffer (ΔNNO; O'Neill and Pownceby, 1993) for Mg-rich calcic amphiboles ($Mg/(Mg+Fe^{2+}) > 0.5$), allowing the estimation of relative oxygen fugacity (fO_2) in log units from Mg#. The hornblende crystals analysed in this study yield ΔNNO values between -0.12 and +0.58, indicating moderately oxidizing crystallisation conditions, comparable to those typical of calc-alkaline magmas (Carmichael, 1991; Martel *et al.,* 1999; Behrens and Gaillard, 2006).

The pressure-temperature estimates and moderately oxidizing and hydrous conditions are consistent with compositional, textural and geochemical evidence indicating near-solidus crystallisation of dioritic magma batches at mid-crustal levels with nearly simultaneous crystallisation of plagioclase and hornblende.

5.2. Magma sources and crystallisation processes

The Turonian/Coniacian Petite and Mercurio plutons are mainly composed of diorite, quartz diorite, and tonalite, comprising hornblende (commonly poikilitic) and subordinate biotite, titanite, apatite, zircon, and magnetite-ilmenite pairs. Despite their relatively low SiO_2 contents (49–55 wt%), samples from Petite pluton display low Mg# (42–43), comparable to more felsic rocks of the South Patagonian Batholith and even lower than the tonalite from the Mercurio pluton (63 wt% SiO_2; Mg# = 52). The trace element bulk-rock composition of the diorite-tonalite suites, including Nb-Ta and Ti negative anomalies, are characteristic of arc magmas in subduction zone settings.

Samples from the Petite pluton are characterized by high LREE contents and absence of Eu anomalies whereas the sample from the Mercurio pluton displays a low total REE content with a small positive Eu anomaly. This relationship suggests a particular case of plagioclase fractionation/accumulation. It is well accepted that Eu negative anomalies are related to plagioclase fractionation, which would be expected for intermediate to felsic magmas. However, the absence of Eu anomaly can be attributed either to no fractionation or to accumulation of plagioclase after fractionation, both of which would be consistent with the high Sr concentration (>600 ppm) and Sr/Y ratios (>20) in the analysed samples.

Although it is generally expected that rocks with more evolved or felsic compositions contain higher concentrations of LREE due to fractionation of ferromagnesian minerals (with low partition coefficients for LREE), the hornblende-biotite tonalite from Mercurio pluton presents a lower LREE concentration than Petite pluton samples. This suggests that the two plutons record coeval yet compositionally distinct magmatic reservoirs at depth. Accordingly, the diorites of the Petite pluton cannot be considered parental to the Mercurio tonalite by simple line of descent.

Textural and compositional evidence in the hornblende diorite from the Petite pluton, such as the occurrence of labradorite plagioclase inclusions within hornblende which in turn exhibits negative Eu anomalies (0.50–0.74), supports early crystallisation of plagioclase and subsequent amphibole and plagioclase co-crystallisation. The combination of low Mg# together with variable low Eu/Eu* ratios in hornblende further suggests that the parental magmas of the diorite formed at depth by extraction of pyroxene, with involvement of plagioclase during early stages of differentiation. Compared with hornblendites and granitoids of the Fuegian Patagonian Batholith (Torres García *et al.,* 2020), the diorites of the Petite pluton could have been produced by crystal accumulation from partially evolved magmas, reflecting advanced melt differentiation rather than direct derivation from primitive mantle-like sources as in the case of the hornblendites (Torres García *et al.,* 2020; Fig. 6). Hornblendites with interstitial plagioclase are characteristic of lower crustal conditions (Torres García *et al.,* 2020), whereas co-crystallisation of hornblende and plagioclase, as observed in the Petite pluton, seems to be more common at mid- and upper crustal levels.

In this sense, the absence of Eu anomaly in samples from the Petite pluton and the subtle positive Eu anomaly of the Mercurio pluton are best interpreted as resulting from late plagioclase accumulation following earlier fractionation, rather than from non-fractionation. Likewise, the lack of correlation between SiO_2 and Mg#, together with the variable enrichment in REE (with the same pattern shape), can be likely interpreted as due to variable ferromagnesian accumulation during late stages of crystallisation rather than a signal inherited from parental magmas or from the source.

5.3. Tectonic implications

The Turonian/Coniacian crystallisation ages of the Petite and Mercurio plutons correlate with regional geochronological data reported in plutonic rocks of the South Patagonian and Fuegian batholiths (see figure 1A; Hervé *et al.,* 2007a; Klepeis *et al.,* 2010; Velásquez *et al.,* 2023). They could be considered part of the Beagle Plutonic Complex (~115–80 Ma; *sensu* Hervé *et al.,* 1984), which in its type locality (Isla Navarino; Fig. 1A) intrudes sedimentary rocks and ophiolitic complexes of the Rocas Verdes Basin, as is the case of the Castores Plutonic Complex of pre- to syn-tectonic gabbroic to tonalitic plutons emplaced at ca. 90–87 Ma (Velásquez *et al.,* 2023).

The emplacement of the Petite and Mercurio plutons locally constrains the minimum age of deformation within an accretionary wedge developed during tectonic underthrusting associated with the closure of the Rocas Verdes marginal basin (Fig. 7). In the study area (Isla Capitán Aracena), which lies within the Scotia Plate south of the Magallanes-Fagnano Fault System, the exposed accretionary sequences consist of thrust and folded basalts and turbidites, with the development of penetrative cleavage in zones proximal to fold hinges (Otzen, 1987, and field observations from Seno Mercurio). In contrast, north of the fault system, the fold-and-thrust belt is characterized by rocks exhibiting brittle-ductile deformation and well-developed mylonitic shear zones, formed at depths of ~20 km under low-to-intermediate temperature conditions (Galaz *et al.,* 2005; Hervé *et al.,* 2007b; Calderón *et al.,* 2011; Muller *et al.,* 2021). These rocks are intruded by ~80 Ma plutons emplaced at depths of ~12 km (Calderón *et al.,* 2007; Muller *et al.,* 2021), indicating that arc magmatism persisted for ~10 Myr in the hinterland of the Magallanes fold-and-thrust belt. However, the duration of magmatism overall spans approximately 25 Myr, between 100 and 75 Ma, based on the geochronological record of plutonic complexes from the Cordillera Sarmiento, the Estrecho de Magallanes, the Cordillera Darwin, and Isla Navarino (see figure 1A; Calderón *et al.,* 2007; Hervé *et al.,* 2007a; Klepeis *et al.,* 2010; Fosdick *et al.,* 2011; Muller *et al.,* 2021; Velásquez *et al.,* 2023).

We propose that tectonic transport towards the continent and progressive deformation of the detached island-arc and oceanic (ophiolitic) remnants were accommodated by folding and thrusting along the interface between the arc-ophiolite assemblage and the continental margin (Fig. 7). This tectonic evolution ultimately led to crustal thickening and flexural loading of the foreland, giving rise to the development of the Magallanes-Austral foreland basin.

6. Concluding remarks

The integrated petrological, geochemical, and geochronological dataset demonstrates that the Petite and Mercurio satellite plutons record Turonian/Coniacian arc magmatism during the closure of the Rocas Verdes back-arc basin within the hinterland of the Magallanes fold-and-thrust belt. Thermobarometric estimates indicate near-solidus crystallisation of hydrous dioritic magmas at shallow crustal levels (~10 km) under moderately oxidizing, water-rich conditions, consistent with calc-alkaline arc environments. Bulk-rock geochemistry, including LILE enrichment and negative Nb-Ta-Ti anomalies, indicates their derivation from a metasomatized mantle wedge modified by slab-derived fluids and/or melts, while contrasting REE signatures and mineralogical evidence reveal the presence of coeval yet compositionally distinct magma reservoirs. The Petite and Mercurio plutons are interpreted to have formed by variable degrees of plagioclase and ferromagnesian phases accumulation from relatively evolved magmas.

U-Pb zircon crystallisation ages (ca. 90 Ma) constrain the timing of deformation within an accretionary wedge, indicating that oceanic and arc-derived crustal fragments of the Rocas Verdes basin were already tectonically buried and deformed at mid-crustal depths by Turonian/Coniacian times. These results highlight the temporal and spatial overlap between arc magmatism and contractional deformation during basin inversion, supporting a model of progressive closure driven by tectonic underthrusting of continental crust. The coupled tectono-magmatic evolution documented here ultimately led to crustal thickening, flexural loading, and the onset of the Magallanes-Austral foreland basin, providing new constraints on the timing and mechanisms of back-arc basin closure and tectonic emplacement of ophiolitic complexes along the southwestern Gondwana margin.

Acknowledgements

Over more than six decades, Francisco “Pancho" Hervé has played a central role in pioneering studies on the igneous and metamorphic complexes of Patagonia and the Antarctic Peninsula. His vision and mentorship have profoundly influenced the Chilean geological community and the regional understanding of continental growth and accretionary processes along southwestern Gondwana. As former students and colleagues, we are particularly indebted to his guidance and scientific rigour, which have shaped both this contribution and our broader approach to the geology of the Patagonian Andes. We thank Robert Pankhurst for editorial handling, and Othmar Müntener and David Peate are thanked for their thoughtful comments, which led to significant improvements in the paper. This work is dedicated to the memory of Moritz Schmelz, who, in addition to participating in the field campaign during which the samples analysed in this study were collected, carried out meticulous, almost jewelry-like work in preparing all the polished sections that have been analysed over decades by Professor Hervé and his collaborators. Funding resources were provided by Fondecyt Regular grants Nº 1211906 and 1161818 (M. Calderón).

References

Allen, R. B. (1982). Geología de la Cordillera Sarmiento, Andes Patagónicos, entre los 51° 00'y 52° 15'lat. S, Magallanes, Chile. Servicio Nacional de Geología y Minería, Boletín, 38, 1–46.

Behrens, H., & Gaillard, F. (2006). Geochemical aspects of melts: Volatiles and redox behavior. Elements, 2(5), 275–280.

Black, L.P., Kamo, S.L., Allen, C.M., Aleinikoff, J.N., Davis, D.W., Korsch, R.J. & Foudoulis, C. (2003). TEMORA 1: a new zircon standard for Phanerozoic U–Pb geochronology. Chemical Geology 200, 155-170.

Betka, P., Klepeis, K., & Mosher, S. (2015). Along-strike variation in crustal shortening and kinematic evolution of the base of a retroarc fold-and-thrust belt: Magallanes, Chile 53° S–54° S. Bulletin, 127(7–8), 1108–1134.

Bruhn, R. L., Stern, C. R., & De Wit, M. J. (1978). Field and geochemical data bearing on the development of a Mesozoic volcano-tectonic rift zone and back-arc basin in southernmost South America. *Earth and Planetary Science Letters*, *41*(1), 32-46.

Calderón, M., Fildani, A., Hervé, F., Fanning, C. M., Weislogel, A., & Cordani, U. (2007). Late Jurassic bimodal magmatism in the northern sea-floor remnant of the Rocas Verdes basin, southern Patagonian Andes. Journal of the Geological Society, 164(5), 1011–1022.

Calderón, M., Fosdick, J., Warren, C., Fanning, C.M., Massonne, H.-J., Fadel Cury, L., Schwanethal, J., Fonseca, P., Galaz, G., Gaytán, D., & Hervé, F. (2012). The low-grade Canal de las Montañas Shear Zone and its role in the tectonic emplacement of the Sarmiento Ophiolitic Complex and Late Cretaceous Patagonian Andes orogeny, Chile. Tectonophysics 244-245, 165-185.

Calderón, M., Prades, C. F., Hervé, F., Avendaño, V., Fanning, C. M., Massonne, H.-J., Theye, T., & Simonetti, A. (2013). Petrological vestiges of the Late Jurassic-Early Cretaceous transition from rift to back-arc basin in southernmost Chile: New age and geochemical data from the Capitán Aracena, Carlos III, and Tortuga ophiolitic complexes. Geochemical Journal, 47(2), 201–217.

Carmichael, I.S.E. (1991). The redox states of basic and silicic magmas: a reflection of their source regions? Contribution to Mineralogy and Petrology, 106, 129-141.

Cunningham, W. D. (1993). Strike-slip faults in the southernmost andes and the development of the Patagonian orocline. Tectonics, 12, 169–186. https://doi.org/10.1029/92TC01790

Dalziel, I. W., de Wit, M. J., & Palmer, K. F. (1974). Fossil marginal basin in the southern Andes. Nature, 250(5464), 291–294.

Dalziel, I. (1981). Back-arc extension in the southern Andes: A review and critical reappraisal. Philosophical Transactions of the Royal Society of London. Series A, Mathematical and Physical Sciences, 300(1454), 319–335.

Davidson, J., Turner, S., Handley, H., Macpherson, C., & Dosseto, A. (2007). Amphibole “sponge” in arc crust? Geology, 35(9), 787–790.

D’Orazio, M., Agostini, S., Innocenti, F., Haller, M. J., Manetti, P., & Mazzarini, F. (2001). Slab window-related magmatism from southernmost South America: The Late Miocene mafic volcanics from the Estancia Glencross Area (52 S, Argentina–Chile). Lithos, 57(2–3), 67–89.

Dott Jr, R. H., Winn Jr, R. D., de Wit, M. J., & Bruhn, R. L. (1977). Tectonic and sedimentary significance of Cretaceous Tekenika Beds of Tierra del Fuego. Nature, 266(5603), 620–622.

Ewart, A. (1982). The mineralogy and petrology of Tertiary Recent orogenic volcanic rocks: With special reference to the andesite-basaltic compositional range. Andesites: Orogenic Andesites and Related Rocks, 25–87.

Fildani, A., & Hessler, A. M. (2005). Stratigraphic record across a retroarc basin inversion: Rocas Verdes–Magallanes basin, Patagonian Andes, Chile. Geological Society of America Bulletin, 117(11–12), 1596–1614.

Fosdick, J. C., Romans, B. W., Fildani, A., Bernhardt, A., Calderón, M., & Graham, S. A. (2011). Kinematic evolution of the Patagonian retroarc fold-and-thrust belt and Magallanes foreland basin, Chile and Argentina, 51 30′ S. Bulletin, 123(9-10), 1679-1698.

Galaz, G., Hervé, F. & Calderón, M. (2005). Metamorfismo y deformación de la Formación Tobífera en la Cordillera Riesco, región de Magallanes, Chile: evidencias para su evolución tectónica. Revista Asociación Geológica Argentina, 60, 4, 762-774.

Gallardo, R., Ghiglione, M., Rojas, L., & Mpodozis, C. (2022). From rift to foreland basin: A case example from the Magallanes-Austral basin, southernmost Andes. Basin Reseaarch 35 (1).

Hammarstrom, J.M. & Zen, E-AN. (1986). Aluminum in hornblende: An empirical igneous geobarometer. Amierican Mineralogist, 71, 1297-1313.

Hervé, F., Pankhurst, R. J., Fanning, C. M., Calderón, M., & Yaxley, G. M. (2007a). The South Patagonian batholith: 150 my of granite magmatism on a plate margin. Lithos, 97(3–4), 373–394.

Hervé, F., Massonne, H-J., Calderón, M. & Theye, T. (2007b). Metamorphic P-T conditions of Late Jurassic rhyolites in the Magallanes fold and thrust belt, Patagonian Andes. Journal of Iberian Geology 33 (1), 5-16.

Hervé, F., Fanning, C.M., Pankhurst, R.J., Mpodozis, C., Klepeis, K., Calderón, M. & Thomson, S.N. (2010). Detrital zircon SHRIMP U–Pb age study of the Cordillera Darwin Metamorphic Complex of Tierra del Fuego: sedimentary sources and implications for the evolution of the Pacific margin of Gondwana. Journal of the Geological Society of London 167, 555-568.

Hervé, M., Suárez, M., & Puig, A. (1984). The Patagonian Batholith S of Tierra del Fuego, Chile: Timing and tectonic implications. Journal of the Geological Society, 141(5), 909–917. https://doi.org/10.1144/gsjgs.141.5.0909

Holland, T., & Blundy, J. (1994). Non-ideal interactions in calcic amphiboles and their bearing on amphibole-plagioclase thermometry. Contributions to Mineralogy and Petrology, 116(4), 433–447.

Ireland, T. R., Clement, S., Compston, W., Foster, J. J., Holden, P., Jenkins, B., Lanc, P., Schram, N., & Williams, I. S. (2008). Development of SHRIMP. Australian Journal of Earth Sciences, 55(6–7), 937–954. https://doi.org/10.1080/08120090802097427

Katz, H. R., & Watters, W. A. (1966). Geological investigation of the Yahgan Formation (Upper Mesozoic) and associated igneous rocks of Navarino Island, Southern Chile. New Zealand Journal of Geology and Geophysics, 9(3), 323–359.

Klepeis, K., Betka, P., Clarke, G., Fanning, M., Hervé, F., Rojas, L., Mpodozis, C., & Thomson, S. (2010). Continental underthrusting and obduction during the Cretaceous closure of the Rocas Verdes rift basin, Cordillera Darwin, Patagonian Andes. Tectonics, 29(3), 2009TC002610.

Leake, B. E., Woolley, A. R., Arps, C. E., Birch, W. D., Gilbert, M. C., Grice, J. D., & Youzhi, G. (1997). Nomenclature of amphiboles; report of the subcommittee on amphiboles of the International Mineralogical Association, Commission on New Minerals and Mineral Names. *The Canadian Mineralogist*, *35*(1), 219-246.

Locock, A. J. (2014). An Excel spreadsheet to classify chemical analyses of amphiboles following the IMA 2012 recommendations. Computers & Geosciences, 62, 1–11.

Ludwig K.R.(2001). SQUID 1.02, A User's Manual; Berkeley Geochronology Center Special Publication. No. 2, 2455 Ridge Road, Berkeley, CA 94709, USA.

Ludwig, K.R. (2003). User's manual for ISOPLOT/EX, Version 3.0, A geochronological toolkit for Microsoft Excel. Berkeley Geochronology Center Special Publication No. 4, 2455 Ridge Road, Berkeley CA 94709, USA.

Martel, C., Pichavant, M., Boudier, J.-L., Traiuneau, H., Holtz, F., Scaillet, B. (1999). Magma storage conditions and control of eruption regime in silici volcanoes: experimental evidence from Mt. Pelée. Earth and Planetary Science Letters, 156, 88-99.

Massonne, H.-J., Opitz, J., Theye, T., & Nasir, S. (2013). Evolution of a very deeply subducted metasediment from As Sifah, northeastern coast of Oman. Lithos, 156, 171–185.

Muller, V. A., Calderón, M., Fosdick, J. C., Ghiglione, M. C., Cury, L. F., Massonne, H.-J., Fanning, C. M., Warren, C. J., de Arellano, C. R., & Sternai, P. (2021). The closure of the Rocas Verdes Basin and early tectono-metamorphic evolution of the Magallanes fold-and-thrust belt, southern Patagonian Andes (52–54° S). Tectonophysics, 798, 228686.

Mutch, E. J. F., Blundy, J. D., Tattitch, B. C., Cooper, F. J., & Brooker, R. A. (2016). An experimental study of amphibole stability in low-pressure granitic magmas and a revised Al-in-hornblende geobarometer. Contributions to Mineralogy and Petrology, 171(10), Article 10. https://doi.org/10.1007/s00410-016-1298-9

O'Neill, H. S. C., & Pownceby, M. I. (1993). Thermodynamic data from redox reactions at high temperatures. I. An experimental and theoretical assessment of the electrochemical method using stabilized zirconia electrolytes, with revised values for the Fe-"FeO", Co-CoO, Ni-NiO and Cu-Cu2O oxygen buffers, and new data for the W-WO2 buffer. Contributions to Mineralogy and Petrology, 114(3), 296–314.

Otzen, G. (1987). Geología Regional de la isla Capitán Aracena y Clarence, Magallanes, Chile. Informe Técnico ENAP (Unpublished Report).

Palme, H., & O'Neill, H. (2014). Cosmochemical Estimates of Mantle Composition. Planets, Asteriods, Comets and The Solar System, Volume 2 of Treatise on Geochemistry. Edited by Andrew M. Davis. Elsevier.

Pankhurst, R. J., Riley, T. R., Fanning, C. M., & Kelley, S. P. (2000). Episodic silicic volcanism in Patagonia and the Antarctic Peninsula: Chronology of magmatism associated with the break-up of Gondwana. Journal of Petrology, 41(5), 605–625.

Pietranik, A., Holtz, F., Koepke, J., & Puziewicz, J. (2009). Crystallization of quartz dioritic magmas at 2 and 1 kbar: Experimental results. Mineralogy and Petrology, 97(1), 1–21.

Polzunenkov, G. O. (2018). Evaluation of P–T and f O2 Conditions of Crystallization of Monzonitic Rocks of the Velitkenay Granite–Migmatite Massif (Arctic Chukotka) Based on Mineral Thermobaro-and Oxybarometry. Russian Journal of Pacific Geology, 12(5), 429–442.

Putirka, K. (2016). Amphibole thermometers and barometers for igneous systems and some implications for eruption mechanisms of felsic magmas at arc volcanoes. American Mineralogist, 101(4), 841–858.

Ramírez-de-Arellano, C., Calderón, M., Rivera, H., Valenzuela, M., Fanning, C. M. & Paredes, E. (2021). Neogene Patagonian magmatism between the rupture of the Farallon plate and the Chile Ridge subduction. Journal of South American Earth Sciences, 110, 103238. https://doi.org/10.1016/j.jsames.2021.103238

Ramírez-de-Arellano, C., Putlitz, B., Müntener, O. & Ovtcharova, M. (2012). High precision U/Pb zircon dating of the Chaltén Plutonic Complex (Cerro Fitz Roy, Patagonia) and its relationship to arc migration in the southernmost Andes. Tectonics, 31(4). https://doi.org/10.1029/2011tc003048

Ridolfi, F., & Renzulli, A. (2012). Calcic amphiboles in calc-alkaline and alkaline magmas: Thermobarometric and chemometric empirical equations valid up to 1,130° C and 2.2 GPa. Contributions to Mineralogy and Petrology, 163(5), 877–895.

Schmidt, M. W. (1993). Phase relations and compositions in tonalite as a function of pressure: An experimental study at 650°C. American Journal of Science, 293, 1011–1060.

Stevens Goddard, A.L., Fosdick, J.C., Calderón, M., Ghiglione, M.C., VanderLeest, R.A., & Romans, B.W. (2023). Thermochronological evidence for Eocene deformation in the southern Patagonian Andes: linking orogenesis along the Patagonian Orocline. Tectonics. 42, e2022TC007677. https://doi.org/10.1029/2022TC007677

Sernageomin, 2003. Mapa Geológico de Chile: digital version. Geological Base scale 1:1.000.000. Chile Government. Servicio Nacional de Geología y Minería.

Stern, C. R., & De Wit, M. J. (2003). Rocas Verdes ophiolites, southernmost South America: Remnants of progressive stages of development of oceanic-type crust in a continental margin back-arc basin. Geological Society of London, Special Publications 218, 665–683.

Torres Carbonell, P.J., Cao, S.J., González Guillot, M., Mosqueira González, V., Dimieri, L.V. & Scaillet, S. (2020). The Fuegian thrust-fold belt: From arc-continent collision to thrust-related deformation in the southernmost Andes, Journal of South American Earth Sciences, 102, 102678.

Torres García, M. F., Calderón, M., Ramírez de Arellano, C., Hervé, F., Opitz, J., Theye, T., Fanning, C. M., Pankhurst, R. J., González-Guillot, M., Fuentes, F., & Babinski, M. (2020). Trace element composition of amphibole and petrogenesis of hornblendites and plutonic suites of Cretaceous magmatic arcs developed in the Fuegian Andes, southernmost South America. Lithos, 372–373, 105656.

Velásquez, R., Bastías-Silva, J., Salazar, E., Poblete, F., Guillot, M. G., Chew, D., Peña, M., Tapia, F., Ramirez, A., & Drakou, F. (2023). Magmatic arc evolution during the tectonic closure of the Rocas Verdes basin: Insights from Cretaceous–earliest Paleocene intrusive rocks of Navarino Island (55° S), Fuegian Andes. Journal of the Geological Society, 180(5), jgs2022-163.

Williams, I.S., 1998, U-Th-Pb geochronology by Ion Microprobe, in McKibben, M.A., Shanks III, W.C., and Ridley, W.I., eds., Application of microanalytical techniques to understanding mineralizing processes. Reviews of Economic Geology 7, Society of Economic Geologists, p. 1–35.

Wilson, T. (1991). Transition from back-arc to foreland basin development in the southernmost Andes: Stratigraphic record from the Ultima Esperanza District, Chile. *Geological Society of America Bulletin*, 103(1), 98-111.

Figure Captions

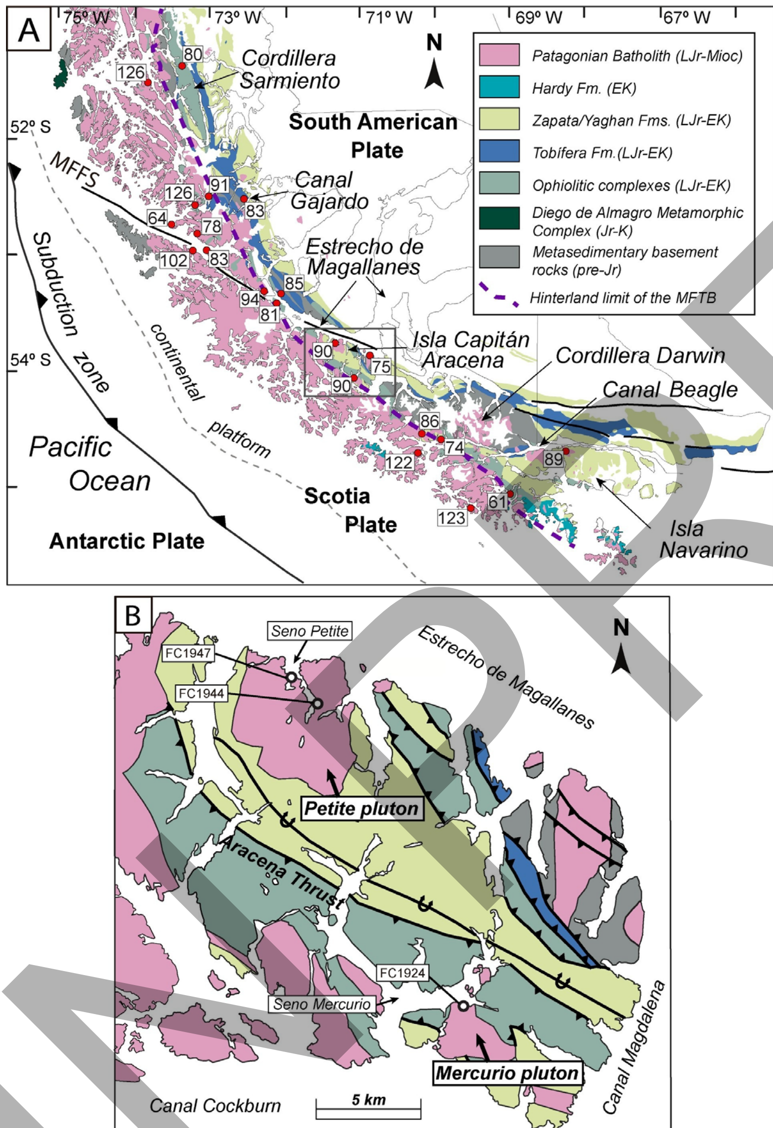

Fig. 1. A. Simplified geological map of the southernmost Andes (modified from Sernageomin, 2003). Zircon U-Pb crystallisation ages are shown (red dots, mean values; data from Hervé et al., 2007a; Calderón et al., 2007; Klepeis et al., 2010; Torres García et

al., 2020; Muller et al., 2021; Velásquez et al., 2023). **B.** Geological map of Isla Capitán Aracena with the locations of samples that were collected from the Petite and Mercurio plutons (see location in A). MFFS: Magallanes-Fagnano Fault System. MFTB: Magallanes Fault-and-Thrust Belt. Jr: Jurassic. K: Cretaceous. LJr: Late Jurassic. EK: Early Cretaceous. Mioc: Miocene.

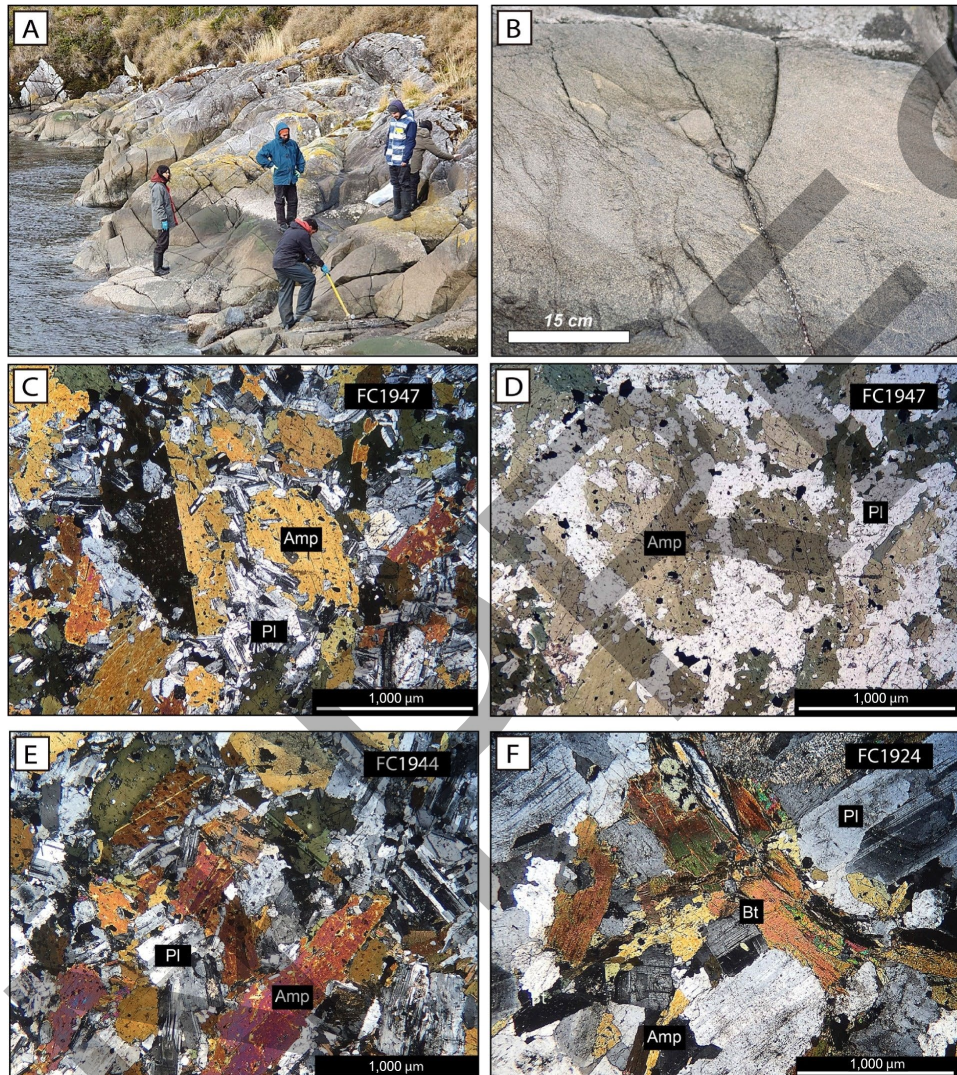

Fig. 2. A. Field photo of the group working on the Petite pluton. **B.** Medium-grained hornblende diorite of the Petite pluton showing compositional banding with preferred orientation of leucocratic segregations bands. **C-F.** Photomicrographs of representative areas of samples illustrating the variety of mineral assemblages and textures of analysed samples. Amp: amphibole, Bt: biotite, Pl: plagioclase.

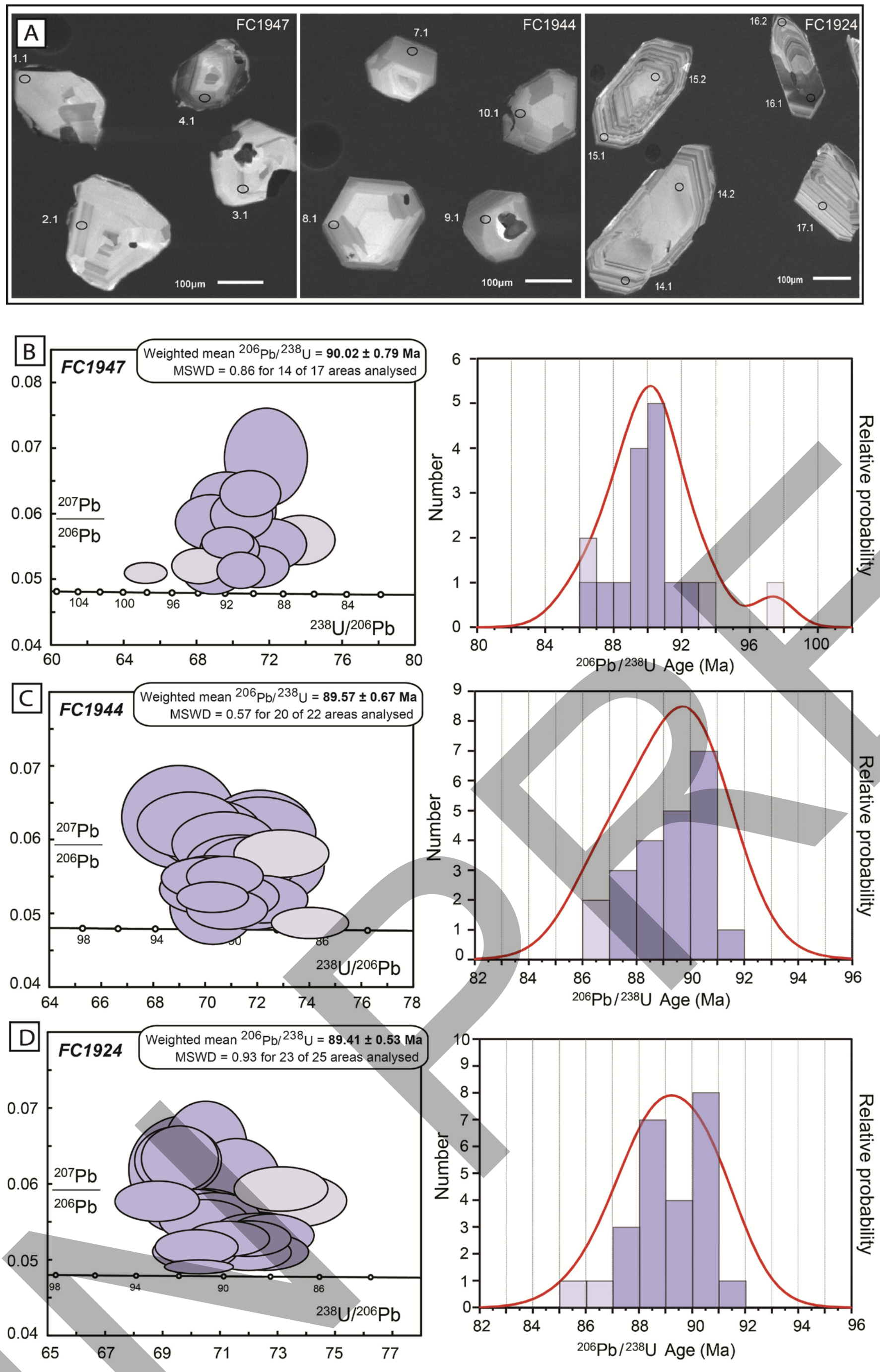

Fig. 3. A. Cathodoluminescence images of dated zircons showing their morphologies and internal structures. **B-D.** Weighted SHRIMP U-Pb zircon data. Tera-Wasserburg concordia (error ellipses at 1σ) and probability density plots for (B) FC1947 (Hornblende diorite), (C) FC1944 (Hornblende quartz diorite), and (D) FC1924 (Hornblende-biotite tonalite). MSWD: Mean Square Weighted Deviation.

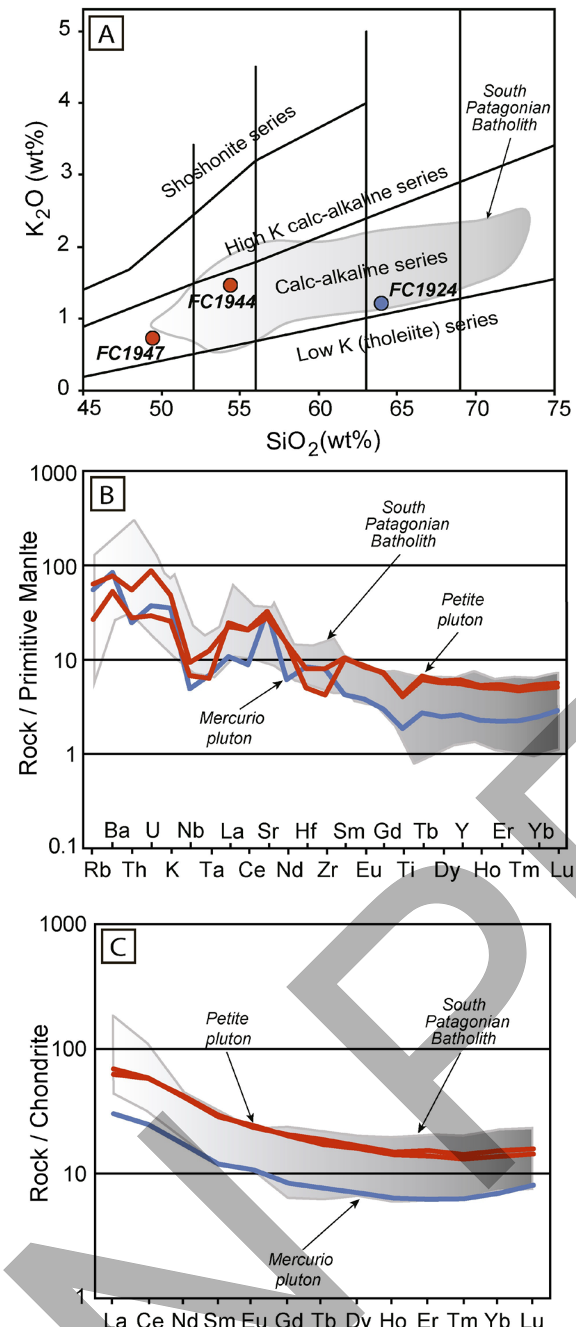

Fig. 4. Bulk-rock and trace element geochemistry of the Petite and Mercurio plutons. The grey field is the data from Hervé et al. (2007a). **A.** K_2O-SiO_2 diagram (Ewart, 1982). **B-C.** Diagrams of bulk-rock trace and REEs normalized to primitive mantle and chondrite, respectively (Palme and O'Neill, 2014).

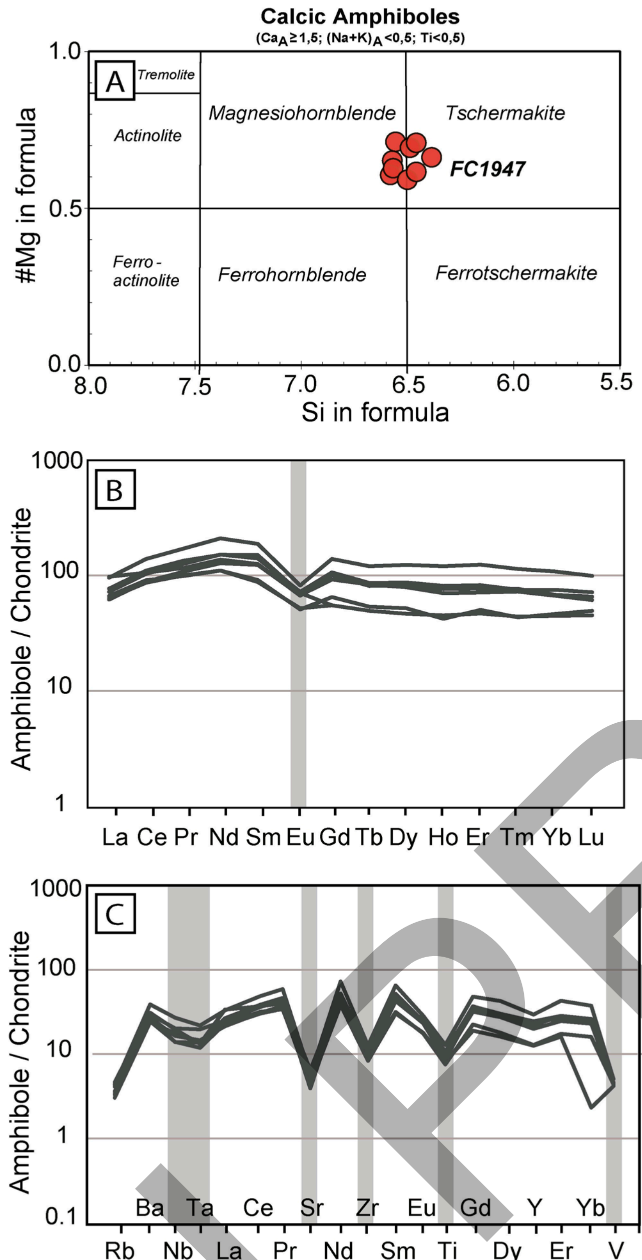

Fig. 5. Amphibole major and trace element covariation plots for sample FC1947 (Petite pluton). **A.** Amphibole classification after Locock (2014) and Leake et al. (1997). **B-C.** Chondrite-normalized REE and incompatible element patterns, respectively. Normalization values are from Palme and O'Neill, 2014.

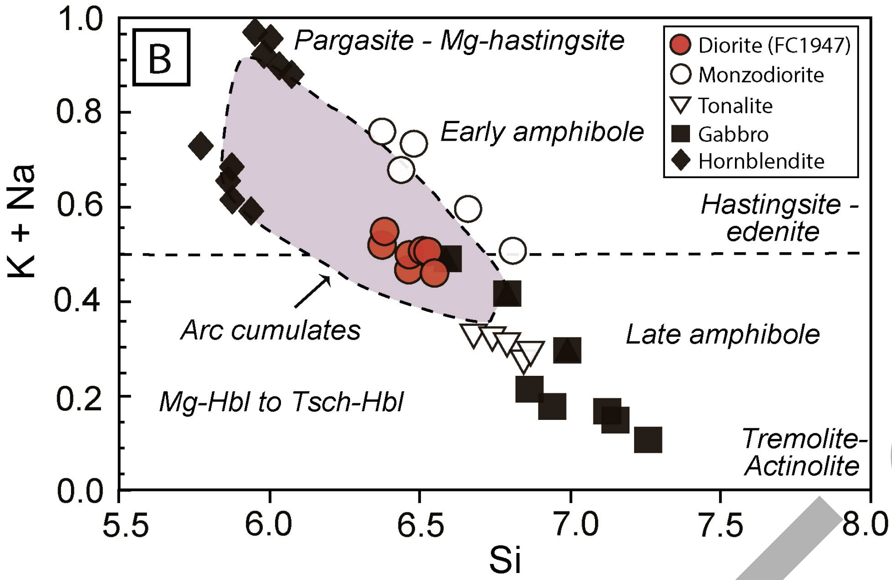

Fig. 6. Si (a.p.f.u) vs Na+K (a.p.f.u) in Ca amphibole diagram. Modified from Torres García et al. (2020), including their compositional database of amphiboles other than for FC1947.

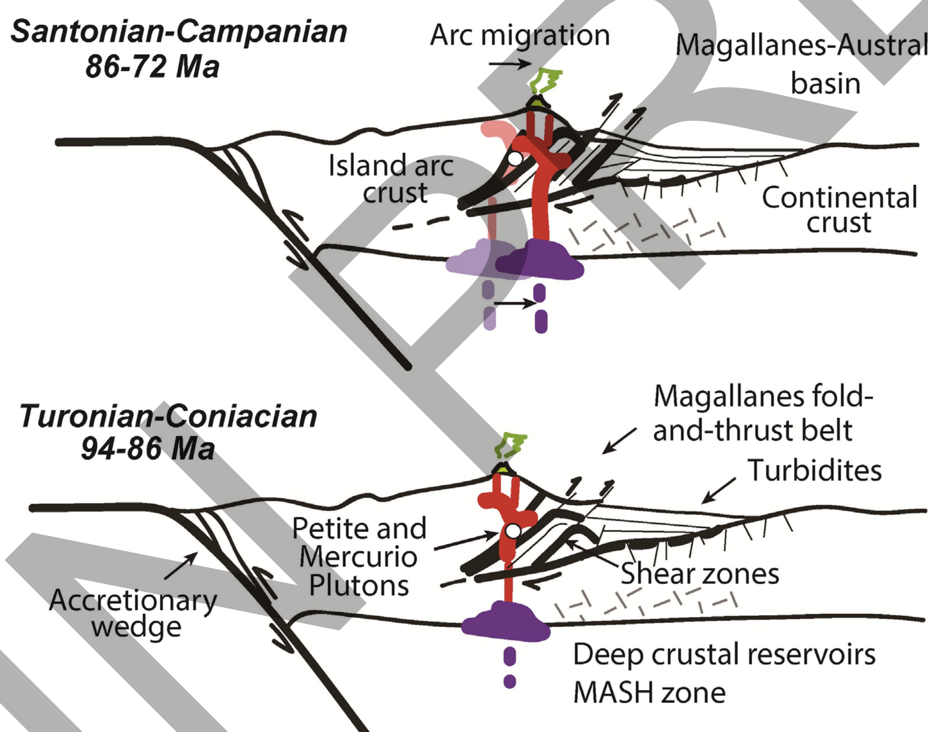

Fig. 7. Schematic reconstruction model for the origin and crustal emplacement of the Petite and Mercurio plutons during the Late Cretaceous stages of Rocas Verdes marginal-basin closure. MASH: Melting, Assimilation, Storage, and Homogenisation.